

A General Model for Pointing Error of High Frequency Directional Antennas

Mohammad. T. Dabiri, Mazen Hasna, *Senior Member, IEEE*, Nizar Zorba, *Senior Member, IEEE*, Tamer Khattab, *Senior Member, IEEE*, and Khalid Qaraqe, *Senior Member, IEEE*

Abstract—This paper focuses on providing an analytical framework for the quantification and evaluation of the pointing error for a general case at high-frequency millimeter wave (mmWave) and terahertz (THz) communication links. For this aim, we first derive the the probability density function (PDF) and cumulative distribution functions (CDF) of the pointing error between an unstable transmitter (Tx) and receiver (Rx), that have different antenna patterns and for which the vibrations are not similar in the Yaw and Pitch directions. The special case where the Tx and Rx are both equipped with uniform linear array antenna is also investigated. In addition, using $\alpha - \mu$ distribution, which is a valid model for small-scale fading of mmWave/THz links, the end-to-end PDF and CDF of the considered channel is derived for all the considered cases. Finally, by employing Monte-Carlo simulations, the accuracy of the analytical expressions is verified and the performance of the system is studied.

Index Terms—Antenna pattern, antenna misalignment, back-haul links, pointing errors, mmWave, THz systems.

I. INTRODUCTION

IN the quest to increase network capacity, high-frequency millimeter wave (mmWave) and terahertz (THz) communication links are widely considered to be one of the next frontiers for future wireless systems, because of the wide swaths of unused and unexplored spectrum. While the mmWave frequencies are already considered in 5G, the vendors and operators have started to look at the usage of the enormous bandwidth of higher THz frequencies [1] and [2]. To mitigate the negative effects of the high path-loss at the mmWave/THz bands, the small wavelength enables the realization of a compact form of highly directive antenna arrays, which also allow a better spatial reuse [3] and [4]. This is an important feature for aerial and even space nodes such as low- and high-altitude unmanned aerial vehicles (UAVs), and low earth orbit (LEO) satellites, which are in great needs of large data rates. Therefore, one of the attractive scenarios is to use the large available bandwidth at mmWave/THz frequencies in order to provide extra data rate for point-to-point aerospace communications.

One of the main challenges of the tackled scenario is mobility, making the high-directional mmWave/THz antennas suffer from transceivers antenna misalignment, known as pointing error for aerial/mobile nodes. Therefore, along with

Mohammad Taghi Dabiri, Mazen Hasna, Nizar Zorba, and Tamer Khattab are with the Department of Electrical Engineering, Qatar University, Doha, Qatar. (E-mail: m.dabiri@qu.edu.qa; hasna@qu.edu.qa; nizarz@qu.edu.qa; tkhattab@ieee.org).

Khalid A. Qaraqe is with the Department of Electrical and Computer Engineering, Texas A&M University at Qatar, Doha 23874, Qatar (E-mail: khalid.qaraqe@qatar.tamu.edu).

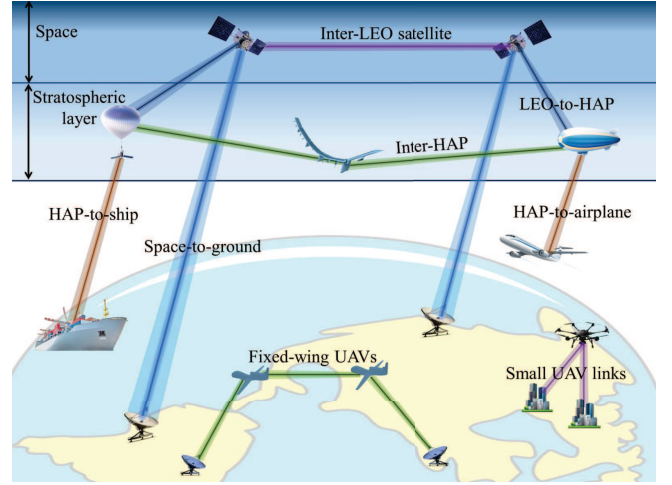


Fig. 1. A nominal illustration of the next generation of aerial networks includes a large number of high-frequency and ultra-high data rates between aerial nodes that require the use of directional antennas.

other research topics in mmWave/THz bands, studying the effect of pointing errors on system performance is a necessity for establishing a high reliable communication link, which has recently been the subject of several studies [5]–[13]. In summary, in [5]–[12], the well-known pointing error model provided in [14] is used, which, although suitable for optical communication systems and a special case of mmWave/THz systems, as we will show in this work, cannot be directly used for the typical mmWave/THz communication systems.

More recently, in [13] a new pointing error model is provided for mmWave/THz communication links in the presence of an unstable transmitter (Tx) and receiver (Rx) nodes as a function of real antennas' pattern. However, the results of [13] are obtained for a very special case where the intensity of the vibrations of both Tx and Rx is the same in the direction of Yaw and Pitch, and also the Tx and Rx nodes have the same antenna pattern with the same stability. However, as shown in Fig. 1, the Tx and Rx nodes are not necessarily of the same type, not necessarily at the same altitude and atmospheric conditions, and as a result, their instability is not the same. As an example, for a communication link between a small multi-rotor UAV and a balloon, it is clear that their instability is different, and more importantly, because the balloon is capable of carrying more payload, it is possible to use a larger antenna for the balloon. In addition, the intensity of the angular vibrations of the nodes is not necessarily the same

in the directions of Yaw and Pitch. For example, although for some types of hovering UAVs the intensity of vibrations in both directions of Yaw and Pitch is almost the same, for fixed-wing UAVs or airplanes, the intensity of vibrations in the direction of Pitch is greater than the intensity of vibrations in the direction of Yaw. Therefore, the model provided in [13] is used only in the special scenario where the Tx and Rx are perfectly symmetric, standing as a major drawback if wanted to use in practical systems. In order to design and analyze the mmWave/THz connections between the moving nodes, it seems necessary to provide a general and tractable model for pointing errors based on the severity of Tx and Rx vibrations, which is the main contribution of this work.

In this work, we consider a general case between two unstable Tx and Rx nodes that are completely asymmetric, meaning that they have different antenna patterns and the vibrations of the nodes are not necessarily the same in the directions of Yaw and Pitch. For the considered general scenario, we derive the probability density function (PDF) and the cumulative distribution functions (CDF) of pointing error by taking into account the 3D real antenna pattern. We show that the obtained closed-form models are completely different from the pointing error models of an optical link, and therefore, the pointing error models of the optical channels cannot be directly used to model the pointing error of mmWave/THz links. Then, for a special case that the standard deviation (SD) of vibrations are approximately equal in the directions of Yaw and Pitch, we derive a more tractable model for the PDF and CDF of pointing error. Notice that, for the special case where the Tx and Rx nodes are completely symmetric (meaning that the SD of vibrations of Tx and Rx nodes along with the antenna pattern are the same), the pointing error models provided in this work reduce to the simple pointing error model provided in [13]. In some situations, such as communications between Low-altitude UAVs, the use of a uniform linear array (ULA) antenna in the direction perpendicular to the ground can have several advantages compared to the planar array antenna. Therefore, for the case where the Tx and Rx are equipped with ULA antennas, we also derive the PDF and CDF of pointing error. In addition, using $\alpha - \mu$ distribution, which is a valid model for small-scale fading of higher frequencies (i.e., mmWave and THz links), the end-to-end PDF and CDF of the considered channel are derived for all the mentioned cases. Finally, by employing Monte-Carlo simulations, the accuracy of the analytical expressions is verified and the performance of the system is studied.

The remainder of the paper is structured as follows. In Section II, the channel of a point-to-point communication link between two unstable Tx and Rx is characterized. The analytical derivations for pointing error are provided in Section III along with several numerical and simulation results to verify the accuracy of the derivations. In Section IV, the analytical derivations for the end-to-end channel are provided for different scenarios. At the end of Section IV, by providing several simulation and analytical results, the performance of the considered system is studied. Finally, conclusions are drawn in Section V.

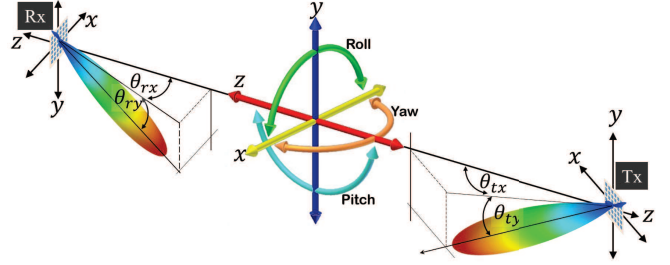


Fig. 2. Graphical illustration of pointing errors of two directional antennas which are mounted on an unstable Tx and Rx. The relationship between the axes of the Cartesian coordinate system and the roll, Yaw, and Pitch directions are depicted in the considered system model.

II. THE SYSTEM MODEL

Consider an optical receiver where a lens is used to focus the incoming received signal onto the small detector or feed antenna located at the focal point. In this case, if the center of received Gaussian beam deviates by d_v from the center of the receiver lens, the fraction of the collected power by the circular lens with radius a (called the pointing error) is calculated as [14], [15]

$$h_p = \int_{-a}^a \int_{-\sqrt{a^2-x^2}}^{\sqrt{a^2-x^2}} \frac{2}{\pi w_z^2} \exp\left(-2\frac{(x-d_v)^2+y^2}{w_z^2}\right) dx dy, \quad (1)$$

where w_z is the beamwidth of the received Gaussian beam. Using Eq. (1) and after a series of manipulations, the distribution of h_p is derived in [14, Eq. (11)]. As mentioned earlier, in the pointing error studies of THz communications, it is typical to refer to [14, Eq. (11)] in order to model the pointing error. Although this model is suitable for FSO systems and/or a specific class of high frequency communication links that use a circular lens in the receiver, in this work, we show that this model is not an accurate model for Lens-less mmWave/THz communication systems.

Consider Fig. 2, where we tackle a point-to-point high frequency communication system between two unstable nodes, and where Tx and Rx are equipped with high directional antennas. The channel model can be written as [16], [17]

$$h = h_L h_a \sqrt{G_t(\theta_t, \phi_t) G_r(\theta_r, \phi_r)}, \quad (2)$$

where $G_q(\theta_q, \phi_q)$ is the antenna radiation pattern defined in Eq. (4), h_a is the small scale fading, $h_L = h_{Lf} h_{Lm}$ is the channel path loss, $h_{Lf} = \left(\frac{\lambda}{4\pi Z}\right)^2$ is the free-space path loss, and $h_{Lm} = e^{-\frac{\mathcal{K}(f)}{2} Z}$ denotes the molecular absorption loss where $\mathcal{K}(f)$ is the frequency dependent absorption coefficient. The experimental results show that water vapor dominates the molecular absorption loss at high frequencies [18]. In mmWave/THz channels, the $\alpha - \mu$ distribution is one of the most widely used models employed for the distribution function of random variables (RV) h_a which is given as [19]

$$f_{h_a}(h_a) = \frac{\alpha \mu^\mu}{\hat{h}_a^{\alpha \mu} \Gamma(\mu)} h_a^{\alpha \mu - 1} \exp\left(-\mu \frac{h_a^\alpha}{\hat{h}_a^\alpha}\right), \quad (3)$$

where $\Gamma(\cdot)$ is the Gamma function, $\alpha > 0$ is a fading parameter, μ is the normalized variance of the fading channel

envelope, and \hat{h}_a is the α -root mean value of the fading channel envelope.

In Eq. (2), the parameter $G_q(\theta_q, \phi_q)$ is the antenna radiation pattern in the directions of θ_q and ϕ_q where the subscript $q \in \{t, r\}$ determines the Tx and Rx nodes. Here, we consider a standard uniform $N \times N$ array antenna. By taking into account the effect of all elements [17], the array radiation gain in the direction of θ_q and ϕ_q will be $G_q(\theta_q, \phi_q) = G_0(N_q)G'_q(\theta_q, \phi_q)$, where

$$G'_q(N_q, \theta_q, \phi_q) = \left(\frac{\sin\left(\frac{N_q(kd_x \sin(\theta_q) \cos(\phi_q))}{2}\right)}{N_q \sin\left(\frac{kd_x \sin(\theta_q) \cos(\phi_q)}{2}\right)} \right)^2 \times \frac{\sin\left(\frac{N_q(kd_y \sin(\theta_q) \sin(\phi_q))}{2}\right)}{N_q \sin\left(\frac{kd_y \sin(\theta_q) \sin(\phi_q)}{2}\right)} \right)^2, \quad (4)$$

and $d_x = d_y = \frac{\lambda}{2}$ are the spacing between the elements along the x and y axes, respectively, $k = \frac{2\pi}{\lambda}$ denotes the wave number, $\lambda = \frac{c}{f_c}$ represents the wavelength, f_c denotes the carrier frequency and c is the speed of light. Also, in order to guarantee that the total radiated power of antennas with different N are the same, the coefficient G_0 is defined as

$$G_0(N_q) = \frac{4\pi}{\int_0^\pi \int_0^{2\pi} G'_q(\theta_q, \phi_q) \sin(\theta_q) d\theta_q d\phi_q}. \quad (5)$$

Based on Eq. (4), the maximum value of the antenna gain is equal to $G_0(N)$, which is obtained when $\theta_q = 0$.

As shown in Fig. 2, we assume that the Tx and Rx are located on axis z and at a distance Z from each other, and both the Tx and Rx try to place the main lobe of the antenna pattern on the z axis. The use of mmWave/THz high-gain antennas makes them more sensitive to antenna misalignment or pointing errors, especially for mobile or aerospace communications. The angular fluctuations of each mobile node are modeled in three directions; namely: Yaw, roll, and Pitch. Due to the symmetry in the main-lobe of the antenna pattern in the direction of roll (angle ϕ_q), we can neglect the effect of orientation deviations in the roll direction on the pointing error. Hence, the orientation fluctuations in the Yaw and Pitch directions cause a pointing error. As shown in Fig. 2, orientation deviations in the directions of Yaw and Pitch are equivalent to the orientation deviations in $x - z$ and $y - z$ planes, respectively. Let $\theta_{tx} \sim \mathcal{N}(0, \sigma_{\theta_{tx}})$ and $\theta_{ty} \sim \mathcal{N}(0, \sigma_{\theta_{ty}})$ denote the orientation fluctuations of Tx in $x - z$ and $y - z$ planes, respectively, while $\theta_{rx} \sim \mathcal{N}(0, \sigma_{\theta_{rx}})$ and $\theta_{ry} \sim \mathcal{N}(0, \sigma_{\theta_{ry}})$ denote the orientation fluctuations of Rx in $x - z$ and $y - z$ planes, respectively. Therefore, in our model, the parameters θ_q can be defined as functions of RV θ_{qx} and θ_{qy} as follows:

$$\theta_q = \tan^{-1} \left(\sqrt{\tan^2(\theta_{qx}) + \tan^2(\theta_{qy})} \right). \quad (6)$$

III. POINTING ERROR MODELING

In this section, we first derive the distribution function of pointing error for the general case and then provide more tractable and precise analytical expressions for some specific

cases. Moreover, the accuracy of the derived analytical expressions is verified by Monte-Carlo simulations.

Let's rewrite Eq. (2) as:

$$h = h_L h_a h_p, \quad (7)$$

where $h_p = G_0(N_t, N_r)h'_p$ is the pointing error coefficient, $G_0(N_t, N_r) = \sqrt{G_0(N_t)G_0(N_r)}$ is the maximum antenna gain, and $0 < h'_p < 1$ is the normalized pointing error

$$h'_p = h'_{pt} h'_{pr} = \sqrt{G'_t(N_t, \theta_{tx}, \theta_{ty})} \sqrt{G'_r(N_r, \theta_{rx}, \theta_{ry})}. \quad (8)$$

From Eq. (8), h'_p is a function of N_t and N_r as well as four RVs $\theta_{tx}, \theta_{ty}, \theta_{rx}$, and θ_{ry} .

Let us define parameters $\beta_{qw} = \frac{\sigma_{\theta_{qw}}^2}{w_{Bq}}$ where the subscript $w \in \{x, y\}$ determines the vibrations of Yaw (or $x - z$ plane) and Pitch (or $y - z$ plane), and the subscript $q \in \{t, r\}$ determines the Tx and Rx nodes. Based on this definition, the general scenarios refer to the condition that $\sigma_{\theta_{qw}}$ s and w_{Bq} s (or N_q s) have different values.

Theorem 1. *Under the general condition when the parameters $\sigma_{\theta_{qw}}$ s and w_{Bq} s have different values, the PDF of pointing error is obtained as:*

$$f_{h_p}(h_p) = C_g \frac{h_p^{1/\beta_1 - 1}}{G_0^{1/\beta_1}} \sum_{k=0}^K \frac{\Delta_k \left(-\ln\left(\frac{h_p}{G_0}\right) \right)^{k+1}}{\Gamma(k+2)\beta_1^{k+2}} \quad (9)$$

while its corresponding CDF results in

$$F_{h_p}(h_p) = 1 - \Theta_0 + C_g \left(\frac{h_p}{G_0} \right)^{1/\beta_1} \times \sum_{k=0}^K \sum_{j=0}^{k+1} \frac{\Delta_k}{\Gamma(k+2-j)\beta_1^{k+1-j}} \left(-\ln\left(\frac{h_p}{G_0}\right) \right)^{k+1-j} \quad (10)$$

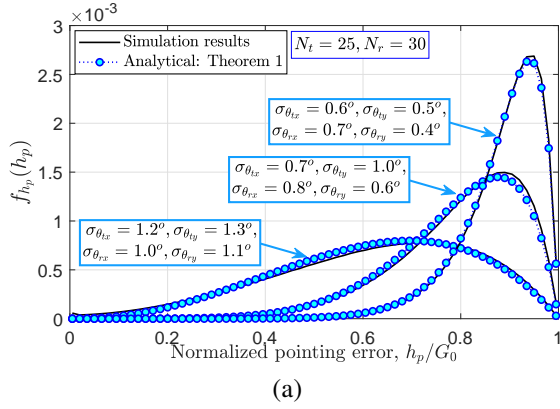
where

$$\begin{cases} C_g = \prod_{i=1}^4 \sqrt{\beta_1/\beta_i}, \\ \Delta_k = \frac{1}{k} \sum_{i=1}^k i \gamma_i \Delta_{k+1-i} \text{ for } k = 1, \dots, K, \\ \Delta_0 = 1, \quad \gamma_k = \sum_{i=1}^4 \frac{(1-\beta_1/\beta_i)^k}{2k}. \end{cases}$$

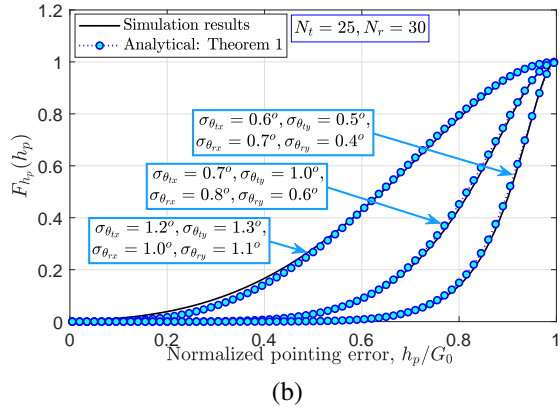
Also, $\bar{\beta} = [\beta_1, \dots, \beta_4]$ where β_1 is the least value of β_{qw} s, β_4 is the maximum value of β_{qw} s, and $\beta_{qw} = \frac{\sigma_{\theta_{qw}}^2}{w_{Bq}}$.

Proof: Please refer to Appendix A. ■

In Fig. 3, by employing Monte-Carlo simulations, we compare the accuracy of the proposed analytical derivations in Theorem 1 for the three different states of transceiver instability. As mentioned, the vibrations of Tx are characterized by $\sigma_{\theta_{tx}}$ and $\sigma_{\theta_{ty}}$, while the vibrations of Rx are characterized by $\sigma_{\theta_{rx}}$ and $\sigma_{\theta_{ry}}$. In the simulations, we use the standard array antenna pattern introduced in Eqs. (4) and (5). To do this, we first generate 5×10^7 independent RVs $\theta_{tx}, \theta_{ty}, \theta_{rx}$, and θ_{ry} , and then, for each 5×10^7 independent run, using Eqs. (4), (5), and (6), we generate 5×10^7 independent RVs of h_p . Next, using the generated instantaneous coefficients h_p s, the PDF and CDF of pointing error are obtained. As can be seen, the Monte-Carlo simulations verify the accuracy of the analytical expressions provided in Theorem 1, especially for low $\sigma_{\theta_{qw}}$



(a)



(b)

Fig. 3. Comparison of the accuracy of the provided analytical results in Theorem 1 with Monte-Carlo simulations for three different states of the intensity of transceiver vibrations (a) for the PDF, and (b) for the CDF.

values. The higher the value of $\sigma_{\theta_{qw}}$, the probability of deviation from the main lobe to the side lobes increases, resulting in a gap between the simulation results and the analytical results. For example, for $N_t = 25$ and $N_r = 30$, although the analytical results for $\sigma_{\theta_{tx}} = 0.6^\circ, \sigma_{\theta_{ty}} = 0.5^\circ, \sigma_{\theta_{rx}} = 0.7^\circ$, and $\sigma_{\theta_{ry}} = 0.4^\circ$ completely match the simulations, by increasing $\sigma_{\theta_{qw}}$ s to $\sigma_{\theta_{tx}} = 1.2^\circ, \sigma_{\theta_{ty}} = 1.3^\circ, \sigma_{\theta_{rx}} = 1.0^\circ$, and $\sigma_{\theta_{ry}} = 1.1^\circ$, it is observed that the analytical results deviate slightly from the simulations.

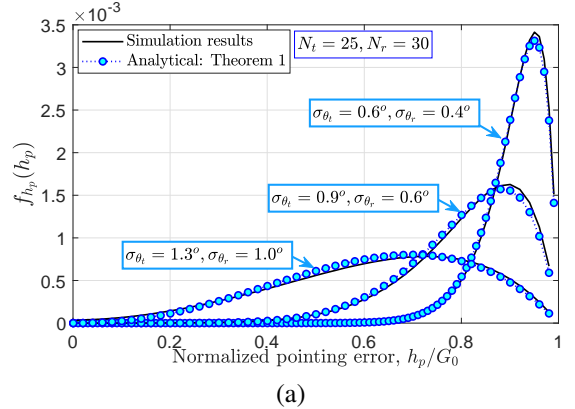
Theorem 2. When $\beta_{tx} = \beta_{ty} = \beta_t$ and $\beta_{rx} = \beta_{ry} = \beta_r$, the PDF and CDF of pointing error are obtained as:

$$f_{h_p}(h_p) = \frac{1}{G_0(\beta_t - \beta_r)} \left[\left(\frac{h_p}{G_0} \right)^{1/\beta_t - 1} - \left(\frac{h_p}{G_0} \right)^{1/\beta_r - 1} \right], \quad (11)$$

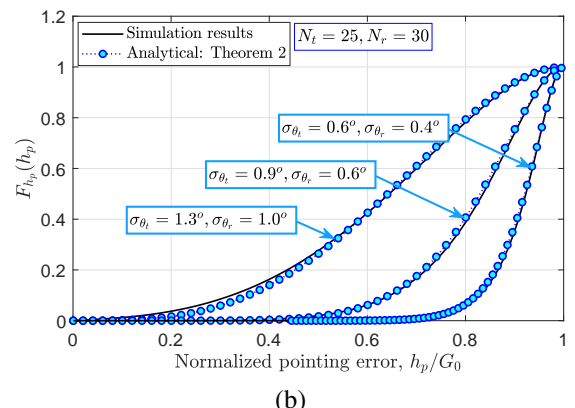
$$F_{h_p}(h_p) = \frac{1}{\beta_t - \beta_r} \left[\beta_t \left(\frac{h_p}{G_0} \right)^{1/\beta_t} - \beta_r \left(\frac{h_p}{G_0} \right)^{1/\beta_r} \right]. \quad (12)$$

Proof: Please refer to Appendix B. ■

The results of Theorem 2 are for a particular case where the severity of vibrations along the Yaw and Pitch directions are approximately the same or $\sigma_{\theta_{tx}} \simeq \sigma_{\theta_{ty}} = \sigma_\theta$ and $\sigma_{\theta_{rx}} \simeq \sigma_{\theta_{ry}} = \sigma_\theta$. For example, for communication between UAVs, when both UAVs are of the same model and at the same altitude, they are expected to have similar fluctuation intensity.



(a)



(b)

Fig. 4. Comparison of the accuracy of the provided analytical results in Theorem 2 with Monte-Carlo simulations for three different states of the intensity of transceiver vibrations (a) for the PDF, and (b) for the CDF.

As we observe from Theorem 2, the closed-form expressions provided in Eqs. (11) and (12) are very tractable and simple. In addition, the simulation results of Fig. 4 verify the accuracy of the analytical expressions under the different values $\sigma_{\theta_{qw}}$ s.

The results of Theorems 1 and 2 are for the planar array antenna. In some situations, such as communications between Low-altitude UAVs, the use of a linear array antenna in the direction perpendicular to the ground (as illustrated in Fig. 5) can have several advantages compared to the planar array antenna. The first important feature of using linear area antenna is that the considered communication link will be resistant to vibrations in the direction of the Yaw or x-z plane. This topology has an approximately flat pattern in the x-z plane and therefore, the vibrations of the UAVs in this direction do not have a significant effect on the system performance. Moreover, this topology has a high-gain pattern in the direction of the Pitch or y-z plane, and thus, interference caused by ground transmitters is reduced significantly, and vice versa. In addition, from an aerodynamic point of view, it is a better option for mounting on UAVs than the planar antennas, especially for fixed-wing UAVs that are in motion.

Theorem 3. When using ULA antennas, the PDF and CDF of pointing error are obtained as:

$$f_{h_p}(h_p) = \frac{1}{\sqrt{\beta_{ty}\beta_{ry}}} G_0^{\frac{2\beta_{ty}\beta_{ry}}{\beta_{ty}+\beta_{ry}}} h_p^{\frac{\beta_{ty}+\beta_{ry}}{2\beta_{ty}\beta_{ry}} - 1}$$

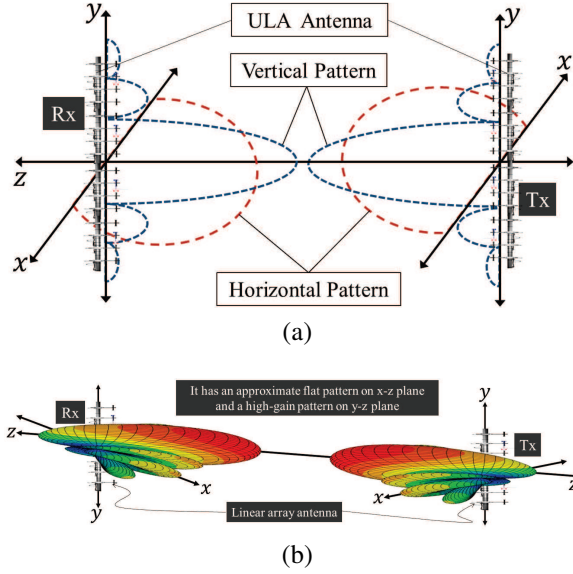


Fig. 5. Illustration of considered configuration based on ULA antenna in such a way that the horizontal pattern, which is almost flat, is horizontal to the ground, and the vertical pattern of the antenna is perpendicular to the ground devices: (a) a better illustration of vertical and horizontal patterns, and (b) a real 3D antenna pattern.

$$\times I_0 \left(\frac{\beta_{ty} - \beta_{ry}}{2\beta_{ty}\beta_{ry}} \ln \left(\frac{h_p}{G_0} \right) \right) \quad (13)$$

$$F_{h_p}(h_p) = 1 - Q \left(\Re_1 \sqrt{\frac{-2 \ln \left(\frac{h_p}{G_0} \right)}{\beta_{ty} + \beta_{ry}}}, \Re_2 \sqrt{\frac{-2 \ln \left(\frac{h_p}{G_0} \right)}{\beta_{ty} + \beta_{ry}}} \right) + Q \left(\Re_2 \sqrt{\frac{-2 \ln \left(\frac{h_p}{G_0} \right)}{\beta_{ty} + \beta_{ry}}}, \Re_1 \sqrt{\frac{-2 \ln \left(\frac{h_p}{G_0} \right)}{\beta_{ty} + \beta_{ry}}} \right) \quad (14)$$

where $Q(a, b)$ is the Marcum Q -function [20], and

$$\begin{cases} \Re_1 = \frac{\sqrt{1-T_q^4}}{2T_q} \sqrt{\frac{1+T_q}{1-T_q}}, \\ \Re_2 = \Re_1 \frac{1-T_q}{1+T_q}, \quad T_q = \frac{\sigma_{\theta_{\min}}}{\sigma_{\theta_{\max}}}, \\ \sigma_{\theta_{\max}} = \max\{\sigma_{\theta_{qx}}, \sigma_{\theta_{qy}}\}, \quad \sigma_{\theta_{\min}} = \min\{\sigma_{\theta_{qx}}, \sigma_{\theta_{qy}}\} \end{cases}$$

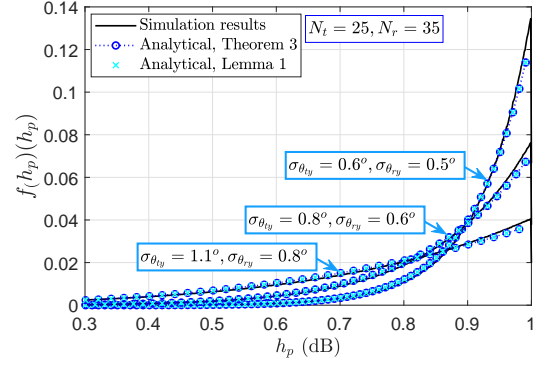
Proof: Please refer to Appendix C. ■

As can be seen, the modified Bessel function of the first kind and the Gamma function have been used in Eqs. (13) and (14). In order to reduce the complexity of calculations, an approximate model is derived below, which uses only a series of simple multiplication and addition operators to model the PDF and CDF of pointing errors.

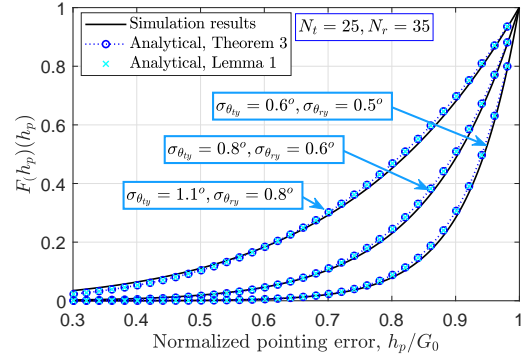
Lemma 1. For linear array antennas, the PDF and CDF of pointing error can be well approximated as:

$$f_{h_p}(h_p) \simeq \sum_{n=1}^N \frac{\Re_4 \Re_5}{\Re_3(n) (\beta_{ty} + \beta_{ry}) G_0} \left(\frac{h_p}{G_0} \right)^{\frac{\Re_4}{\beta_{ty} + \beta_{ry}} - 1} \quad (15)$$

$$F_{h_p}(h_p) \simeq \sum_{n=1}^N \frac{\Re_5}{\Re_3(n)} \left(\frac{h_p}{G_0} \right)^{\frac{\Re_4}{\beta_{ty} + \beta_{ry}}} \quad (16)$$



(a)



(b)

Fig. 6. Comparison of the accuracy of the provided analytical results in Theorem 3 and Lemma 1 for ULA antenna with Monte-Carlo simulations for three different states of the intensity of transceiver vibrations (a) the PDF, and (b) the CDF.

where

$$\begin{cases} \Re_3(n) = 1 + \frac{1-T_q^2}{1+T_q^2} \cos \left(\pi \frac{2n-1}{N} \right), \\ \Re_4 = \frac{(1+T_q^2)^2}{2T_q^2} \Re_3(n), \quad \Re_5 = \frac{2T_q}{N(1+T_q^2)}. \end{cases}$$

Proof: Please refer to Appendix C. ■

The closed-form expressions provided in Lemma 1 are very tractable and simple. In addition, the simulation results of Fig. 6 verify the accuracy of the analytical expressions of Theorem 3 and Lemma 1 under different values $\sigma_{\theta_{qw}}$ s.

In some scenarios, we may have a communication link between a stable node and an unstable node. For example, for a ground-to-UAV or a UAV-to-ground station, the intensity of vibrations of the ground node is negligible compared to the UAV node. In this case, the pointing error model provided in Theorem 3 and Lemma 1 can be used with a series of minor changes that are described in **Remark 1**.

Remark 1. By following the method used in Appendices A and C, it can be easily shown that the analytical expressions in Theorem 3 and Lemma 1 can be used for a ground-to-UAV link by substituting β_{rx} instead of β_{ty} . Also, by substituting β_{tx} instead of β_{ry} , we can use Theorem 3 and Lemma 1 for modeling the pointing error of a UAV-to-ground link.

IV. END-TO-END CHANNEL MODELING AND PERFORMANCE ANALYSIS

The channel path loss, due to free-space propagation and the molecular absorption loss, is a deterministic parameter and does not change the distribution function of the considered channel. However, in addition to the random parameter due to the pointing error, in some high-frequency typologies, we may also have the effect of small-scale fading. Small-scale fading can be caused by various factors such as atmospheric turbulence in rainy weather or multi-path fading for ground links or close to the ground. In this work, we use the $\alpha - \mu$ distribution to model the small-scale fading, which is the most common model for modeling the small-scale fading of high frequency channels. In the sequel, for the pointing error models provided in Theorems 1-3, we derive the end-to-end channel distribution function of the considered communication link in Theorems 4-6 by considering $\alpha - \mu$ distribution for small-scale fading.

Theorem 4. *Under the general condition when the parameters $\sigma_{\theta_{qw}}$ s and w_{Bq} s have different values, the PDF of h is obtained as:*

$$f_h(h) \simeq \frac{A_1 C_g}{2G_0^{\alpha\mu} h_L} \left(\frac{h}{h_L}\right)^{\alpha\mu-1} \sum_{k=0}^K \frac{\Delta_k}{\Gamma(k+2)\beta_1^{k+2}} e^{-\frac{A_1(h)}{\alpha^2}} \times \frac{1}{\mathbb{A}_1(h)^{k/2+1}} \times \left[\Gamma\left(\frac{k+2}{2}\right) {}_1F_1\left(\frac{k+2}{2}, \frac{1}{2}; \frac{A_2(h)}{4}\right) + \frac{\alpha A_3 - \mathbb{A}_1(h)}{\alpha \sqrt{\mathbb{A}_1(h)}} \Gamma\left(\frac{k+3}{2}\right) {}_1F_1\left(\frac{k+3}{2}; \frac{3}{2}; \frac{A_2(h)}{4}\right) \right] \quad (17)$$

where

$$\begin{cases} \mathbb{A}_0(h) = \left(\frac{h}{G_0 h_L}\right)^\alpha, & \mathbb{A}_1(h) = \frac{A_2 \alpha^2}{2} \mathbb{A}_0(h), \\ \mathbb{A}_2(h) = \frac{(A_3 - \mathbb{A}_1(h)/\alpha)^2}{\mathbb{A}_1(h)}, \\ A_1 = \frac{\alpha \mu^\mu}{h_a^{\alpha\mu} \Gamma(\mu)}, & A_2 = \frac{\mu}{h_a}, \quad A_3 = \alpha\mu - 1/\beta_1 \end{cases}$$

Also, the CDF of h is derived as

$$F_h(h) = 1 - C_g \sum_{m=0}^{\mu-1} \sum_{k=0}^K \frac{A_2^m}{\Gamma(m+1)} \frac{\Delta_k}{\Gamma(k+2)\beta_1^{k+2}} \mathbb{A}_0(h)^m \times e^{-A_2 \mathbb{A}_0(h)} \sum_{j=0}^{k+1} 2^{j-k-2} \binom{k+1}{j} \left(m\alpha - \frac{1}{\beta_1} - A_2 \mathbb{A}_0(h)\alpha\right)^{k-j+1} \times \left(\frac{\alpha^2 A_2 \mathbb{A}_0(h)}{2}\right)^{\frac{j-3}{2}-k} \exp\left(\frac{\left(m\alpha - \frac{1}{\beta_1} - A_2 \mathbb{A}_0(h)\alpha\right)^2}{2(\alpha^2 A_2 \mathbb{A}_0(h))}\right) \times \Gamma\left(\frac{j+1}{2}, \frac{\left(m\alpha - \frac{1}{\beta_1} - A_2 \mathbb{A}_0(h)\alpha\right)^2}{2(\alpha^2 A_2 \mathbb{A}_0(h))}\right) \quad (18)$$

Proof: Please refer to Appendix D. ■

Theorem 5. *When $\beta_{tx} = \beta_{ty} = \beta_t$ and $\beta_{rx} = \beta_{ry} = \beta_r$, the PDF and CDF of h are obtained as:*

$$f_h(h) = \frac{1}{\alpha(\beta_t - \beta_r)} \frac{1}{A_2 h_L G_0} A_1 (\mathbb{A}_0(h))^{\mu - \frac{1}{\alpha} - 1} \times \left[(A_2 \mathbb{A}_0(h))^{\frac{V_1}{2}} e^{-\frac{A_2 \mathbb{A}_0(h)}{2}} \mathbb{W}_{-\frac{V_1}{2}, \frac{1-V_1}{2}}(A_2 \mathbb{A}_0(h)) - (A_2 \mathbb{A}_0(h))^{\frac{V_2}{2}} e^{-\frac{A_2 \mathbb{A}_0(h)}{2}} \mathbb{W}_{-\frac{V_2}{2}, \frac{1-V_2}{2}}(A_2 \mathbb{A}_0(h)) \right] \quad (19)$$

and

$$F_h(h) = 1 - \frac{1}{\alpha(\beta_t - \beta_r)} \sum_{k=0}^{\mu-1} \frac{(A_2 \mathbb{A}_0(h))^{k-1}}{\Gamma(k+1)} e^{-\frac{A_2 \mathbb{A}_0(h)}{2}} \times \left[(A_2 \mathbb{A}_0(h))^{\frac{V_3}{2}} \mathbb{W}_{-\frac{V_3}{2}, \frac{1-V_3}{2}}(A_2 \mathbb{A}_0(h)) - (A_2 \mathbb{A}_0(h))^{\frac{V_4}{2}} \mathbb{W}_{-\frac{V_4}{2}, \frac{1-V_4}{2}}(A_2 \mathbb{A}_0(h)) \right] \quad (21)$$

where $\mathbb{W}_{-\frac{v}{2}, \frac{1-v}{2}}(u)$ is the Whittaker function [21], $V_1 = (1/\alpha\beta_t - \mu + 1)$, $V_2 = (1/\alpha\beta_r - \mu + 1)$, $V_3 = (1/\alpha\beta_t - k + 1)$, and $V_4 = (1/\alpha\beta_r - k + 1)$.

Proof: Please refer to Appendix E. ■

Lemma 2. *When $\beta_{tx} = \beta_{ty} = \beta_t$, and $\beta_{rx} = \beta_{ry} = \beta_r$, and under the condition that $(\alpha\mu \min\{\beta_t, \beta_r\}) > 1$, the PDF of h can be approximated as:*

$$f_h(h) = \frac{1}{\alpha(\beta_t - \beta_r)} \frac{A_1 (\mathbb{A}_0(h))^{\mu - \frac{1}{\alpha} - 1}}{A_2 h_L G_0} \times \left[(A_2 \mathbb{A}_0(h))^{1-s_1} \Gamma(s_1, A_2 \mathbb{A}_0(h)) - (A_2 \mathbb{A}_0(h))^{1-s_2} \Gamma(s_2, A_2 \mathbb{A}_0(h)) \right] \quad (22)$$

where $\Gamma(s, x)$, is the upper incomplete gamma function [22], $s_1 = (-1/\alpha\beta_t + \mu)$, and $s_2 = (-1/\alpha\beta_r + \mu)$.

Proof: Please refer to Appendix E. ■

The results of Eq. (22) are based on the upper incomplete gamma function $\Gamma(s, x)$, which has faster computation than the Whittaker function. However, it should be noted that for $\Gamma(s, x)$, the parameter s must be positive. In Eq. (22), both s_1 and s_2 are function of the parameters α and μ related to the small-scale distribution, as well as are function of the parameters β_t and β_r . The parameters β_t and β_r characterize the strength of pointing error. For smaller values of N_q and/or smaller values of $\sigma_{\theta_{qw}}$, the parameters β_t and β_r decrease, and thus, the values of parameters s_1 and s_2 becomes negative. As a results, smaller values of N_q and $\sigma_{\theta_{qw}}$, the results of Lemma 2 are not valid. However, in a wide range of channel parameter values, the results of Lemma 2 are valid.

Theorem 6. *For linear array antenna, the PDF of h is obtained as:*

$$f_h(h) = \sum_{n=1}^N \frac{A_1 \Re_4 \Re_5}{\alpha \Re_3(n)(\beta_{ty} + \beta_{ry})} \frac{1}{A_2 h_L G_0} (\mathbb{A}_0(h))^{\mu-1/\alpha-1} \times (A_2 \mathbb{A}_0(h))^{\frac{V_5}{2}} e^{-\frac{A_2 \mathbb{A}_0(h)}{2}} \mathbb{W}_{-\frac{V_5}{2}, \frac{1-V_5}{2}}(A_2 \mathbb{A}_0(h)) \quad (23)$$

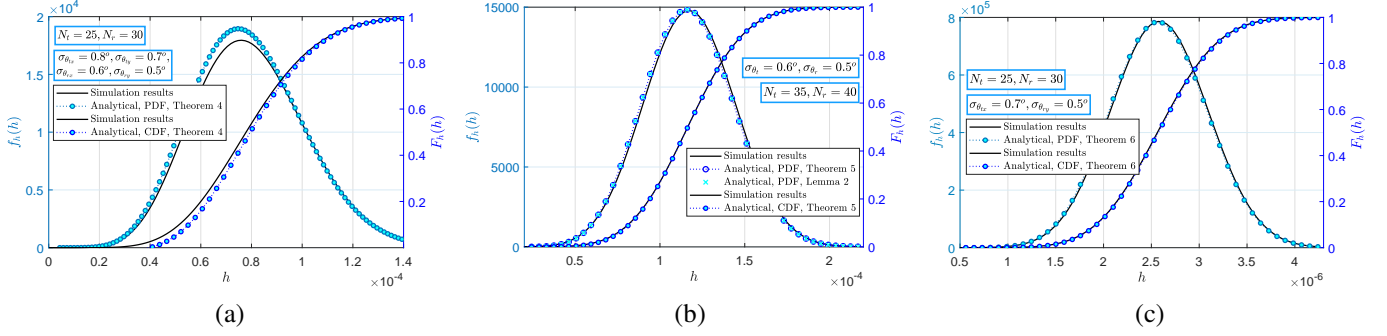


Fig. 7. Comparison of the accuracy of the provided analytical results with Monte-Carlo simulations: (a) for the general scenario provided in Theorem 4, (b) for a special case provided in Theorem 5 and Lemma 2, and (c) for ULA antenna provided in Theorem 6.

and the CDF is calculated as

$$F_h(h) = 1 - \sum_{k=0}^{\mu-1} \sum_{n=1}^N \frac{1}{\alpha \Gamma(k+1)} \frac{\Re_4 \Re_5}{\Re_3(n)(\beta_{ty} + \beta_{ry})} \times (A_2 \mathbb{A}_0(h))^{k + \frac{V_6}{2} - 1} e^{-\frac{A_2 \mathbb{A}_0(h)}{2}} \mathbb{W}_{-\frac{V_6}{2}, \frac{1-V_6}{2}}(A_2 \mathbb{A}_0(h)) \quad (24)$$

where $V_5 = \frac{\Re_4}{\alpha(\beta_{ty} + \beta_{ry})} - \mu + 1$, and $V_6 = \frac{\Re_4}{\alpha(\beta_{ty} + \beta_{ry})} - k + 1$.

Proof: Please refer to Appendix F. ■

In Fig. 7, the accuracy of the analytical expressions provided in Theorems 4-6 is examined using Monte-Carlo simulations. Here, we set $\alpha = 2$, $\mu = 4$, $f_c = 280\text{GHz}$, $\mathcal{K}(f) = 2$, and other parameters related to the antenna pattern and pointing errors, as specified in Fig. 7. According to the result obtained from Fig. 7a, although the analytical results obtained from Theorem 4 are close to the simulation results with an acceptable accuracy, however, a small gap is observed between the simulation results and the results obtained from the approximated analytical expressions in Theorem 2. The results of Figs. 7b and 7c also show that the analytical results obtained from Theorems 5 and 6 completely match the simulation results.

Finally, in Figs. 8 and 9, we evaluate the performance of the considered communication link in term of the outage probability. In the simulations, we set transmit power $P_t = 10\text{mW}$, and SNR threshold $\gamma_{th} = 5\text{dB}$. Also, for computing thermal noise power, we consider bandwidth $\Delta_f = 100\text{MHz}$, and receiver's temperature $T = 300\text{K}$. The results of Fig. 8 are plotted for different values of molecular absorption loss characterized by $\mathcal{K}(f) = 0.5, 1, 2$, and 4 . For example, if we consider that for a quality of service (QoS) with target outage probability lower than 10^{-2} , it is observed that by increasing $\mathcal{K}(f)$ from 0.5 to 4 , the maximum achievable link length to guarantee the requested QoS decreases from 3.1km to lower than 1 km . There are several ways to increase the maximum achievable link-length of the considered system under the presence of molecular absorption loss. However, due to the limited transmission power at higher frequencies, one of the best methods is to increase the gain of the antenna by increasing parameter N . For this aim, the results of Fig. 9 are plotted for different values of N . The results of Fig. 9 show an important point that system performance does not necessarily improve with

increasing N . The reason is that, with increasing antenna gain, the beamwidth of antenna pattern decreases and the system becomes more sensitive to the vibrations of Tx/Rx. To better illustrate this point, the results in Fig. 9 are plotted for two different values for $\sigma_{\theta_{qw}}$ s. The first category is for $\sigma_{\theta_t} = 1^\circ$ and $\sigma_{\theta_r} = 0.8^\circ$. For this state and for target outage probability equal to 10^{-3} , the optimal value is $N = 30$. The second category is for $\sigma_{\theta_t} = 0.4^\circ$ and $\sigma_{\theta_r} = 0.3^\circ$ that we observe the maximum link length is obtained for $N = 60$ in the target outage probability 10^{-3} .

V. CONCLUSIONS

A general pointing error model was investigated for directional mmWave/THz links by taking into account actual antenna patterns. Our derivation is based on the practical assumption that the intensity of instability in Tx and Rx and also the intensity of instability in the Yaw and Pitch directions are different. For lower frequencies as well as higher heights, the small-scale fading effect can be ignored with good accuracy, and as a result, the presented models for pointing errors can be used for end-to-end system analysis. For higher frequencies and in some scenarios, the effect of small-scale fading should be considered. To this end, using $\alpha - \mu$ distribution, which is a common model for small-scale fading of THz links, the end-to-end PDF and CDF of the considered channel are derived for both planer and linear array antennas. The results of this work can be also used to calculate the end-to-end channel distribution in the presence of newer small-scale fading models. Finally, by employing Monte-Carlo simulations, the accuracy of the analytical expressions was verified and the performance of the system was studied.

APPENDIX A

The main lobe of the antenna pattern can be well approximated by the Gaussian distribution function as [13]

$$G_q(N_q, \theta_{qx}, \theta_{qy}) = G_0(N_q) \times \exp\left(-\frac{\left(\tan^{-1}\left(\sqrt{\tan^2(\theta_{qx}) + \tan^2(\theta_{qy})}\right)\right)^2}{w_B^2(N_q)}\right), \quad (25)$$

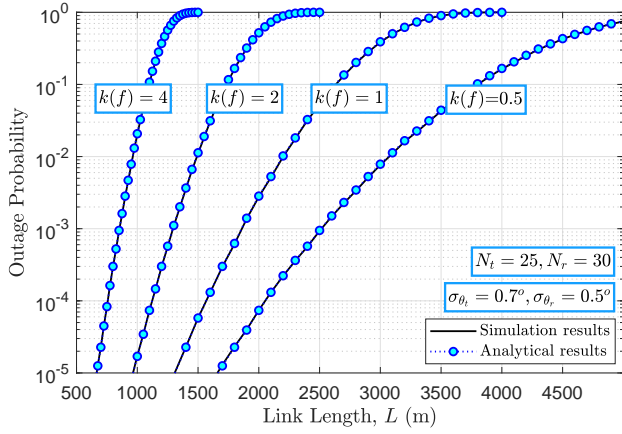


Fig. 8. Outage probability of the considered communication link versus link length for different values of molecular absorption loss characterized by $\mathcal{K}(f)$.

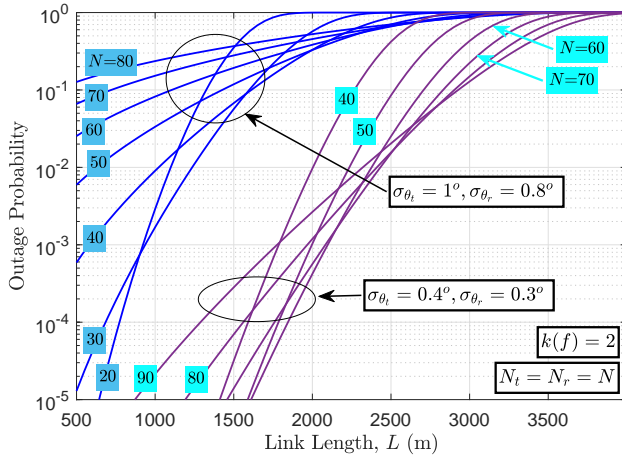


Fig. 9. Outage probability of the considered communication link versus link length for two different levels of system instability and different values for N .

where $G_0(N_q) = \pi N_q^2$, and $w_B(N_q) = \frac{1.061}{N_q}$ is the angular beamwidth (called the beam divergence). For lower values of θ_{qx} and θ_{qy} , we can approximate RV θ_q as

$$\theta_q \simeq \sqrt{\theta_{qx}^2 + \theta_{qy}^2}. \quad (26)$$

Substituting Eqs. (26) and (25) in Eq. (8), we have

$$h_p \simeq G_0(N) \exp\left(-\frac{\theta_{tx}^2 + \theta_{ty}^2}{2w_{Bt}^2} - \frac{\theta_{rx}^2 + \theta_{ry}^2}{2w_{Br}^2}\right) \quad (27)$$

Let us define parameter Θ as

$$\Theta = \Theta_{tx} + \Theta_{ty} + \Theta_{rx} + \Theta_{ry} \quad (28)$$

where $\Theta_{qw} = \frac{\theta_{qw}^2}{2w_{Bq}^2}$. Since $\theta_{qw} \sim \mathcal{N}(0, \sigma_{\theta_{qw}})$, then Θ_{qw} follows a gamma distribution as [23]

$$f_{\Theta_{qw}}(\Theta_{qw}) = \frac{1}{\sqrt{\beta_{qw}\Theta_{qw}}\Gamma(1/2)} \exp\left(-\frac{\Theta_{qw}}{\beta_{qw}}\right) \quad (29)$$

where $\beta_{qw} = \frac{\sigma_{\theta_{qw}}^2}{w_{Bq}^2}$. Let's arrange the parameters β_{qw} s in ascending order and then define the vector $\vec{\beta} = [\beta_1, \dots, \beta_4]$,

where β_1 is the least value of β_{qw} s and β_4 is the maximum value of β_{qw} s. Based on the results of [24, Theorem 1], the distribution of RV Θ is obtained as:

$$f_{\Theta}(\Theta) = C_g \sum_{k=0}^K \frac{\Delta_k \Theta^{k+1} \exp\left(-\frac{\Theta}{\beta_1}\right)}{\Gamma(k+2)\beta_1^{k+2}} \quad (30)$$

where

$$\begin{cases} C_g = \prod_{i=1}^4 \sqrt{\beta_1/\beta_i}, \\ \Delta_k = \frac{1}{k} \sum_{i=1}^k i \gamma_i \Delta_{k+1-i} \text{ for } k = 1, \dots, K, \\ \Delta_0 = 1, \quad \gamma_k = \sum_{i=1}^4 \frac{(1-\beta_1/\beta_i)^k}{2k}. \end{cases}$$

From Eq. (27), the distribution of h_p can be obtained as [23]

$$f_{h_p}(h_p) = f_{\Theta}\left(-\ln\left(\frac{h_p}{G_0}\right)\right) \frac{d\Theta}{dh_p} = \frac{1}{h_p} f_{\Theta}\left(-\ln\left(\frac{h_p}{G_0}\right)\right) \quad (31)$$

Using Eqs. (30) and (31), the closed-form expression for PDF of h_p is derived in Eq. (9).

From Eq. (30), the CDF of RV Θ is obtained as

$$F_{\Theta}(\Theta) = C_g \sum_{k=0}^K \frac{\Delta_k}{\Gamma(k+2)\beta_1^{k+2}} \int_0^{\Theta} x^{k+1} \exp\left(-\frac{x}{\beta_1}\right) \quad (32)$$

In the following derivation, we use an integral identity [21, eq. (2.321.2)]:

$$\int x^n e^{ax} dx = e^{ax} \left(\sum_{j=0}^n \frac{(-1)^j j! \binom{n}{j}}{a^{j+1}} x^{n-j} \right) \quad (33)$$

Using Eq. (33), the CDF of RV Θ is derived as

$$F_{\Theta}(\Theta) = \Theta_0 - C_g e^{-\frac{\Theta}{\beta_1}} \sum_{k=0}^K \sum_{j=0}^{k+1} \frac{\Delta_k \Theta^{k+1-j}}{\Gamma(k+2-j)\beta_1^{k+1-j}} \quad (34)$$

where $\Theta_0 = C_g \sum_{k=0}^K \Delta_k$. Based on Eq. (27), the CDF of h_p is obtained as

$$F_{h_p}(h_p) = \text{Prob}\left\{\Theta > -\ln\left(\frac{h_p}{G_0}\right)\right\} = 1 - F_{\Theta}\left(-\ln\left(\frac{h_p}{G_0}\right)\right) \quad (35)$$

Finally, using Eqs. (34) and (35), the closed-form expression for CDF of h_p is derived in Eq. (10).

APPENDIX B

In this appendix, we obtain the PDF and CDF of h_p for the scenario where the intensity of the vibrations along the Yaw and Pitch axes is the same, approximately. For this case, using Eqs. (8), (25), and (26), the RV h_p can be formulated as

$$h_p \simeq G_0(N) \exp\left(-\frac{\theta_t^2}{2w_{Bt}^2} - \frac{\theta_r^2}{2w_{Br}^2}\right). \quad (36)$$

where $\theta_q = \sqrt{\theta_{qx}^2 + \theta_{qy}^2}$ and since $\theta_{qw} \sim \mathcal{N}(0, \sigma_{\theta_{qw}})$, the RV θ_{qw} follows Rayleigh distribution as [23]

$$f_{\theta_q}(\theta_q) = \frac{\theta_q}{\sigma_{\theta_q}^2} \exp\left(-\frac{\theta_q^2}{2\sigma_{\theta_q}^2}\right) \quad (37)$$

Let us define $\theta_{tr} = \frac{\theta_t^2}{2w_{Bt}^2} + \frac{\theta_r^2}{2w_{Br}^2}$. The CDF of RV θ_{tr} conditioned on θ_r is obtained as:

$$F_{\theta_{tr}|\theta_r}(\theta_{tr}) = \text{Prob} \left\{ \frac{\theta_t^2}{2w_{Bt}^2} + \frac{\theta_r^2}{2w_{Br}^2} < \theta_{tr} | \theta_r \right\} \\ = F_t \left(\sqrt{2w_{Bt}^2 \theta_{tr} - \frac{w_{Bt}^2 \theta_r^2}{w_{Br}^2}} \right) \quad (38)$$

Taking the derivative of Eq. (38) with respect to θ_{tr} , the PDF of RV θ_{tr} conditioned on RV θ_r is obtained as

$$f_{\theta_{tr}|\theta_r}(\theta_{tr}) = \frac{w_{Bt}^2}{\sqrt{2w_{Bt}^2 \theta_{tr} - \frac{w_{Bt}^2 \theta_r^2}{w_{Br}^2}}} \\ \times f_{\theta_t} \left(\sqrt{2w_{Bt}^2 \theta_{tr} - \frac{w_{Bt}^2 \theta_r^2}{w_{Br}^2}} \right) \quad (39)$$

Using Eqs. (37) and (39), and after some manipulations, the PDF of θ_{tr} is derived as

$$f_{\theta_{tr}}(\theta_{tr}) = \frac{w_{Bt}^2 w_{Br}^2}{w_{Br}^2 \sigma_{\theta_t}^2 - w_{Bt}^2 \sigma_{\theta_r}^2} \\ \times \left[\exp \left(-\frac{w_{Bt}^2 \theta_{tr}}{\sigma_{\theta_t}^2} \right) - \exp \left(-\frac{w_{Br}^2 \theta_{tr}}{\sigma_{\theta_r}^2} \right) \right] \quad (40)$$

Now, using Eqs. (31) and (40), and after some derivations, the PDF of pointing error is derived in Eq. (11). By integrating Eq. (40), the CDF of θ_{tr} is obtained as

$$F_{\theta_{tr}}(\theta_{tr}) = \frac{w_{Bt}^2 w_{Br}^2}{w_{Br}^2 \sigma_{\theta_t}^2 - w_{Bt}^2 \sigma_{\theta_r}^2} \left[\frac{\sigma_{\theta_t}^2}{w_{Bt}^2} \left(1 - \exp \left(-\frac{w_{Bt}^2 \theta_{tr}}{\sigma_{\theta_t}^2} \right) \right) \right. \\ \left. - \frac{\sigma_{\theta_r}^2}{w_{Br}^2} \left(1 - \exp \left(-\frac{w_{Br}^2 \theta_{tr}}{\sigma_{\theta_r}^2} \right) \right) \right]. \quad (41)$$

Finally, using Eqs. (35) and (41), and after some derivations, the CDF of h_p is derived in Eq. (12).

APPENDIX C

In this section, we derive the PDF and CDF of h_p for the scenario in which the Tx and Rx are equipped with ULA antennas. For ULA antennas, the antenna pattern model provided in Eq. (4) is simplified as [17]

$$G'_q(N_q, \theta_q, \phi_q) = \left(\frac{\sin \left(\frac{N_q (k d_y \sin(\theta_q) \sin(\phi_q))}{2} \right)}{N_q \sin \left(\frac{k d_y \sin(\theta_q) \sin(\phi_q)}{2} \right)} \right)^2. \quad (42)$$

For this scenario, using Eqs. (8), (25), and (42), the RV h_p is formulated as

$$h_p \simeq G_0 \exp \left(-\frac{\theta_{qx}^2 + \theta_{qy}^2}{2w_{Bq}^2} \right) \quad (43)$$

Let us define $\Theta = \frac{\theta_{qx}^2}{2w_{Bq}^2} + \frac{\theta_{qy}^2}{2w_{Bq}^2}$. Using [25, eqs. (3) and (5)], the distribution of Θ is obtained as

$$f_{\Theta}(\Theta) = \frac{1}{\sqrt{\beta_{qx}\beta_{qy}}} \exp \left(-\frac{\beta_{qx} + \beta_{qy}}{2\beta_{qx}\beta_{qy}} \Theta \right) I_0 \left(\frac{\beta_{qx} - \beta_{qy}}{2\beta_{qx}\beta_{qy}} \Theta \right) \quad (44)$$

where $I_0(\cdot)$ is the modified Bessel function of the first kind with order zero. Using Eqs. (31) and (44), the PDF of h_p is derived as

$$f_{h_p}(h_p) = \frac{1}{\sqrt{\beta_{qx}\beta_{qy}}} G_0^{\frac{2\beta_{qx}\beta_{qy}}{\beta_{qx} + \beta_{qy}}} h_p^{\frac{\beta_{qx} + \beta_{qy}}{2\beta_{qx}\beta_{qy}} - 1} \\ \times I_0 \left(\frac{\beta_{qy} - \beta_{qx}}{2\beta_{qx}\beta_{qy}} \ln \left(\frac{h_p}{G_0} \right) \right) \quad (45)$$

Based on Eq. (45) and using [26], the CDF of Θ is derived as

$$F_{\Theta}(\Theta) = Q \left(\mathfrak{R}_1 \sqrt{\frac{2\Theta}{\beta_{qx} + \beta_{qy}}}, \mathfrak{R}_2 \sqrt{\frac{2\Theta}{\beta_{qx} + \beta_{qy}}} \right) \\ - Q \left(\mathfrak{R}_2 \sqrt{\frac{2\Theta}{\beta_{qx} + \beta_{qy}}}, \mathfrak{R}_1 \sqrt{\frac{2\Theta}{\beta_{qx} + \beta_{qy}}} \right) \quad (46)$$

where where $Q(a, b)$ is the Marcum Q -function, and

$$\begin{cases} \mathfrak{R}_1 = \frac{\sqrt{1-T_q^4}}{2T_q} \sqrt{\frac{1+T_q}{1-T_q}}, \\ \mathfrak{R}_2 = \mathfrak{R}_1 \frac{1-T_q}{1+T_q}, \quad T_q = \frac{\sigma_{\theta_{\min}}}{\sigma_{\theta_{\max}}}, \\ \sigma_{\theta_{\max}} = \max\{\sigma_{\theta_{qx}}, \sigma_{\theta_{qy}}\}, \quad \sigma_{\theta_{\min}} = \min\{\sigma_{\theta_{qx}}, \sigma_{\theta_{qy}}\} \end{cases}$$

Substituting Eq. (46) in Eq. (35), the CDF of h_p is obtained as

$$F_{h_p}(h_p) = 1 - Q \left(\mathfrak{R}_1 \sqrt{\frac{-2 \ln \left(\frac{h_p}{G_0} \right)}{\beta_{qx} + \beta_{qy}}}, \mathfrak{R}_2 \sqrt{\frac{-2 \ln \left(\frac{h_p}{G_0} \right)}{\beta_{qx} + \beta_{qy}}} \right) \\ + Q \left(\mathfrak{R}_2 \sqrt{\frac{-2 \ln \left(\frac{h_p}{G_0} \right)}{\beta_{qx} + \beta_{qy}}}, \mathfrak{R}_1 \sqrt{\frac{-2 \ln \left(\frac{h_p}{G_0} \right)}{\beta_{qx} + \beta_{qy}}} \right) \quad (47)$$

Now in the continuation of this section, we provide simpler analytical expressions for the PDF and CDF of h_p . Using [27, eq. (5)], the CDF of RV Θ can be well approximated as

$$F_{\Theta}(\Theta) \simeq 1 - \sum_{n=1}^N \frac{\mathfrak{R}_5}{\mathfrak{R}_3(n)} \exp \left(-\frac{\mathfrak{R}_4}{\beta_{qx} + \beta_{qy}} \Theta \right) \quad (48)$$

where

$$\begin{cases} \mathfrak{R}_3(n) = 1 + \frac{1-T_q^2}{1+T_q^2} \cos \left(\pi \frac{2n-1}{N} \right), \\ \mathfrak{R}_4 = \frac{(1+T_q^2)^2}{2T_q^2} \mathfrak{R}_3(n), \quad \mathfrak{R}_5 = \frac{2T_q}{N(1+T_q^2)}. \end{cases}$$

Using Eqs. (35) and (47), the CDF of h_p is derived in Eq. (16). Finally, by taking the derivative of Eq. (16), the PDF of h_p is derived in Eq. (15).

APPENDIX D

In this appendix, we obtain the PDF and CDF of h for the considered general scenario. From Eq. (7) and [23], we have

$$f_h(h) = \int_0^{G_0} \frac{1}{h_L h_p} f_{h_a} \left(\frac{h}{h_L h_p} \right) f_{h_p}(h_p) dh_p \quad (49)$$

Substituting Eqs. (3) and (9) in Eq. (49), we obtain:

$$f_h(h) = \frac{A_1 C_g}{G_0} \frac{1}{h_L} \left(\frac{h}{h_L} \right)^{\alpha\mu-1} \sum_{k=0}^K \frac{\Delta_k}{\Gamma(k+2)\beta_1^{k+2}} \times \int_0^{G_0} \exp\left(-A_2 \left(\frac{h}{h_L h_p} \right)^\alpha\right) \frac{h_p^{\frac{1}{\beta_1}-\alpha\mu-1}}{G_0^{1/\beta_1-1}} \left(-\ln\left(\frac{h_p}{G_0}\right)\right)^{k+1} dh_p \quad (50)$$

where $A_1 = \frac{\alpha\mu^\mu}{h_a^{\alpha\mu}\Gamma(\mu)}$, and $A_2 = \frac{\mu}{h_a^\alpha}$. Applying a change of variable rule $x = -\ln\left(\frac{h_p}{G_0}\right)$, we rewrite Eq. (50) as

$$f_h(h) = \frac{A_1 C_g}{G_0^{\alpha\mu}} \frac{1}{h_L} \left(\frac{h}{h_L} \right)^{\alpha\mu-1} \sum_{k=0}^K \frac{\Delta_k}{\Gamma(k+2)\beta_1^{k+2}} \times \int_0^\infty \exp\left(-A_2 \left(\frac{h}{G_0 h_L} \right)^\alpha e^{\alpha x}\right) e^{(\alpha\mu-1/\beta_1)x} x^{k+1} dx \quad (51)$$

It can be easily shown that for $x > \alpha$, the above integral expression tends to zero. Therefore, we can approximate $e^{\alpha x} = 1 + \alpha x + \frac{\alpha^2 x^2}{2}$. Based on this, we approximate Eq. (51) as

$$f_h(h) = \frac{A_1 C_g}{G_0^{\alpha\mu}} \frac{1}{h_L} \left(\frac{h}{h_L} \right)^{\alpha\mu-1} \sum_{k=0}^K \frac{\Delta_k}{\Gamma(k+2)\beta_1^{k+2}} \times \exp\left(-A_2 \left(\frac{h}{G_0 h_L} \right)^\alpha\right) \int_0^\infty e^{-A_3 x^2 + A_4 x} x^{k+1} dx \quad (52)$$

where $A_3 = \left(\frac{A_2}{2} \left(\frac{h}{G_0 h_L}\right)^\alpha \alpha^2\right)$, and $A_4 = \left(\alpha\mu - 1/\beta_1 - A_2 \left(\frac{h}{G_0 h_L}\right)^\alpha \alpha\right)$. In the following derivation, we use an integral identity [21]

$$\int_0^\infty x^n e^{-x^2+bx} dx = \frac{1}{2} \left[b\Gamma\left(\frac{n}{2}+1\right) {}_1F_1\left(\frac{n}{2}+1; \frac{3}{2}; \frac{b^2}{4}\right) + \Gamma\left(\frac{n+1}{2}\right) {}_1F_1\left(\frac{n+1}{2}, \frac{1}{2}, \frac{b^2}{4}\right) \right] \quad (53)$$

Using Eqs. (52) and (53), and after some manipulations, the closed form expressions for the PDF of h is derived in Eq. (17).

From Eq. (7) and [23], we have

$$F_h(h) = \int_0^{G_0} F_{h_a} \left(\frac{h}{h_L h_p} \right) f_{h_p}(h_p) dh_p \quad (54)$$

The CDF of $\alpha - \mu$ distribution can be expressed as [8, eqs. (66) and (67)]

$$F_{h_a}(h_a) = 1 - \sum_{k=0}^{\mu-1} \frac{A_2^k}{\Gamma(k+1)} h_a^{k\alpha} e^{-A_2 h_a^\alpha}. \quad (55)$$

Substituting Eqs. (9) and (55) in Eq. (54), we obtain:

$$F_h(h) = 1 - \frac{C_g}{G_0^{1/\beta_1}} \sum_{m=0}^{\mu-1} \sum_{k=0}^K \frac{A_2^m}{\Gamma(m+1)} \frac{\Delta_k}{\Gamma(k+2)\beta_1^{k+2}} \times \int_0^{G_0} \left(\frac{h}{h_L h_p} \right)^{m\alpha} e^{-A_2 \left(\frac{h}{h_L h_p} \right)^\alpha} h_p^{\frac{1}{\beta_1}-1} \left(-\ln\left(\frac{h_p}{G_0}\right)\right)^{k+1} dh_p \quad (56)$$

Applying a change of variable rule $x = -\ln\left(\frac{h_p}{G_0}\right)$, Eq. (56) is expressed as

$$F_h(h) = 1 - \frac{C_g}{1} \sum_{m=0}^{\mu-1} \sum_{k=0}^K \frac{A_2^m}{\Gamma(m+1)} \frac{\Delta_k}{\Gamma(k+2)\beta_1^{k+2}} \times \int_0^\infty \left(\frac{h}{h_L G_0} \right)^{m\alpha} \exp\left(-A_2 \left(\frac{h}{h_L G_0} \right)^\alpha e^{\alpha x}\right) \times e^{(m\alpha-\frac{1}{\beta_1})x} x^{k+1} dx \quad (57)$$

In the following derivation, we use an integral identity [21]

$$\int_0^\infty x^n e^{ax^2+bx} dx = \sum_{j=0}^n 2^{j-n-1} \binom{n}{j} b^{n-j} (-a)^{\frac{j-1}{2}-n} \times \exp\left(-\frac{b^2}{4a}\right) \Gamma\left(\frac{j+1}{2}, -\frac{b^2}{4a}\right) \quad (58)$$

Finally, using Eqs. (57) and (58), and after some manipulations, the closed-form expression for the CDF of h is derived in Eq. (18).

APPENDIX E

In this appendix, we obtain the PDF and CDF of h for the case where the intensity of the vibrations along the Yaw and Pitch axes is the same, approximately. Substituting Eqs. (3) and (11) in Eq. (49), we obtain:

$$f_h(h) = \frac{A_1}{G_0(\beta_t - \beta_r)} \int_0^{G_0} \frac{1}{h_L h_p} \times \left(\frac{h}{h_L h_p} \right)^{\alpha\mu-1} \exp\left(-A_2 \left(\frac{h}{h_L h_p} \right)^\alpha\right) \times \left(\left(\frac{h_p}{G_0} \right)^{1/\beta_t-1} - \left(\frac{h_p}{G_0} \right)^{1/\beta_r-1} \right) dh_p \quad (59)$$

Applying a change of variable rule $x = \left(\frac{h_p}{G_0}\right)^{-\alpha}$, Eq. (59) is rewritten as

$$f_h(h) = \frac{1}{\alpha(\beta_t - \beta_r)} \frac{1}{h_L G_0} A_1 (\mathbb{A}_0(h))^\mu e^{-\frac{1}{\alpha}} \times \int_1^\infty \exp(-A_2 \mathbb{A}_0(h)x) \left(x^{-1/\alpha\beta_t+\mu-1} - x^{-1/\alpha\beta_r+\mu-1}\right) dx \quad (60)$$

In the following derivation, we use an integral identity [21]

$$\int_u^\infty x^{-\nu} e^{-x} dx = u^{-\nu/2} e^{-u/2} \mathbb{W}_{-\frac{\nu}{2}, \frac{1-\nu}{2}}(u) \quad (61)$$

Using Eqs. (60) and (61), the closed-form expressions for the PDF of h is derived in Eq. (19). Note that the results of Eq. (19) are based on the Whittaker function. If $(\alpha\mu \min\{\beta_t, \beta_r\}) > 1$, we can express Eq. (19) based on the upper incomplete gamma function $\Gamma(s, x)$, which has faster computation than the Whittaker function. Using Eq. (60) and [22], and after some derivation, the closed-form expressions for the PDF of h is derived in Eq. (22).

Substituting Eqs. (19) and (55) in Eq. (54), we obtain:

$$F_h(h) = 1 - \frac{1}{G_0(\beta_t - \beta_r)} \sum_{k=0}^{\mu-1} \frac{A_2^k}{\Gamma(k+1)} \int_0^{G_0} \left(\frac{h}{h_L h_p} \right)^{k\alpha} \times \exp \left(-A_2 \left(\frac{h}{h_L h_p} \right)^\alpha \right) \left[\left(\frac{h_p}{G_0} \right)^{1/\beta_t - 1} - \left(\frac{h_p}{G_0} \right)^{1/\beta_r - 1} \right] dh_p \quad (62)$$

Applying a change of variable rule $x = \left(\frac{h_p}{G_0} \right)^{-\alpha}$ and using Eqs. (61) and (62), the closed-form expressions for the CDF of h is derived in Eq. (20).

APPENDIX F

In this section, we derive the PDF and CDF of h for the case in which the Tx and Rx are equipped with ULA antenna. Substituting Eqs. (3) and (23) in Eq. (49), we obtain:

$$f_h(h) = \sum_{n=1}^N \frac{A_1 \Re_4 \Re_5}{\Re_3(n)(\beta_{ty} + \beta_{ry})G_0} \int_0^{G_0} \frac{1}{h_L h_p} \left(\frac{h}{h_L h_p} \right)^{\alpha\mu-1} \times \exp \left(-A_2 \left(\frac{h}{h_L h_p} \right)^\alpha \right) \left(\frac{h_p}{G_0} \right)^{\frac{\Re_4}{\beta_{ty} + \beta_{ry}} - 1} dh_p \quad (63)$$

Also, substituting Eqs. (23) and (55) in Eq. (54), we obtain:

$$F_h(h) = 1 - \sum_{k=0}^{\mu-1} \sum_{n=1}^N \frac{\Re_4 \Re_5}{\Re_3(n)(\beta_{ty} + \beta_{ry})} \frac{A_2^k \left(\frac{h}{G_0 h_L} \right)^{\alpha k}}{\Gamma(k+1)} \times \int_0^1 \exp \left(-A_2 \left(\frac{h}{G_0 h_L} \right)^\alpha y^{-\alpha} \right) y^{-k\alpha + \frac{\Re_4}{\beta_{ty} + \beta_{ry}} - 1} dy \quad (64)$$

Using Eqs. (63) and (64) and similar to the method used in Appendix E, the closed-form expressions for the PDF and CDF of h are derived in Eqs. (23) and (24), respectively.

REFERENCES

- [1] D. Moltchanov, E. Sopin, V. Begishev, A. Samuylov, Y. Koucheryavy, and K. Samouylov, "A tutorial on mathematical modeling of 5G/6G millimeter wave and terahertz cellular systems," *IEEE Communications Surveys & Tutorials*, 2022.
- [2] V. Petrov, D. Moltchanov, Y. Koucheryavy, and J. M. Jornet, "Capacity and outage of terahertz communications with user micro-mobility and beam misalignment," *IEEE Trans. Veh. Technol.*, vol. 69, no. 6, pp. 6822–6827, 2020.
- [3] H. Chen, H. Sameddeen, T. Ballal, H. Wymeersch, M.-S. Alouini, and T. Y. Al-Naffouri, "A tutorial on terahertz-band localization for 6G communication systems," *IEEE Communications Surveys & Tutorials*, 2022.
- [4] H. Sameddeen, M.-S. Alouini, and T. Y. Al-Naffouri, "An overview of signal processing techniques for terahertz communications," *Proceedings of the IEEE*, 2021.
- [5] O. S. Badarneh, "Performance analysis of tera-hertz communications in random fog conditions with misalignment," *IEEE Wireless Commun. Let.*, 2022.
- [6] P. Bhardwaj and S. M. Zafaruddin, "Performance of dual-hop relaying for THz-RF wireless link over asymmetrical α - μ fading," *IEEE Transactions on Vehicular Technology*, vol. 70, no. 10, pp. 10 031–10 047, 2021.
- [7] H. Du, J. Zhang, K. Guan, D. Niyato, H. Jiao, Z. Wang, and T. Kürner, "Performance and optimization of reconfigurable intelligent surface aided THz communications," *IEEE Transactions on Communications*, 2022.
- [8] A.-A. A. Boulogeorgos, E. N. Papatotiriou, and A. Alexiou, "Analytical performance assessment of THz wireless systems," *IEEE Access*, vol. 7, pp. 11 436–11 453, 2019.
- [9] X. Tong, B. Chang, Z. Meng, G. Zhao, and Z. Chen, "Calculating terahertz channel capacity under beam misalignment and user mobility," *IEEE Wireless Communications Letters*, 2021.
- [10] A.-A. A. Boulogeorgos, A. Alexiou, and M. Di Renzo, "Outage performance analysis of RIS-assisted UAV wireless systems under disorientation and misalignment," *arXiv preprint arXiv:2201.12056*, 2022.
- [11] A.-A. A. Boulogeorgos, J. M. Riera, and A. Alexiou, "On the joint effect of rain and beam misalignment in terahertz wireless systems," *IEEE Access*, 2022.
- [12] S. Liu, X. Yu, R. Guo, Y. Tang, and Z. Zhao, "THz channel modeling: Consolidating the road to THz communications," *China Communications*, vol. 18, no. 5, pp. 33–49, 2021.
- [13] M. T. Dabiri and M. Hasna, "Pointing error modeling of mmWave to THz high-directional antennas," *arXiv preprint arXiv:2206.10756*, 2022.
- [14] A. A. Farid and S. Hranilovic, "Outage capacity optimization for free-space optical links with pointing errors," *J. Lightw. technol.*, vol. 25, no. 7, pp. 1702–1710, 2007.
- [15] M. T. Dabiri, S. M. S. Sadough, and M. A. Khalighi, "Channel modeling and parameter optimization for hovering UAV-based free-space optical links," *IEEE J. Sel. Areas Commun.*, vol. 36, no. 9, pp. 2104–2113, 2018.
- [16] J. Kokkonen, A.-A. A. Boulogeorgos, M. Aminu, J. Lehtomäki, A. Alexiou, and M. Juntti, "Impact of beam misalignment on THz wireless systems," *Nano Commun. Netw.*, vol. 24, p. 100302, 2020.
- [17] C. A. Balanis, *Antenna theory: analysis and design*. John Wiley & sons, 2016.
- [18] S. Tripathi, N. V. Sabu, A. K. Gupta, and H. S. Dhillon, "Millimeter-wave and terahertz spectrum for 6G wireless," in *6G Mobile Wireless Netw.* Springer, 2021, pp. 83–121.
- [19] E. N. Papatotiriou, A.-A. A. Boulogeorgos, K. Haneda, M. F. de Guzman, and A. Alexiou, "An experimentally validated fading model for THz wireless systems," *Scientific Reports*, vol. 11, no. 1, pp. 1–14, 2021.
- [20] E. W. Weisstein, "Marcum q-function." From MathWorld—A Wolfram Web Resource. [Online]. Available: <https://mathworld.wolfram.com/MarcumQ-Function.html>
- [21] I. S. Gradshteyn and I. M. Ryzhik, *Table of integrals, series, and products*. 7th ed. Academic press, 2007.
- [22] E. W. Weisstein, "Incomplete gamma function." From MathWorld—A Wolfram Web Resource.
- [23] A. Papoulis and S. U. Pillai, *Probability, random variables, and stochastic processes*. Tata McGraw-Hill Education, 2002.
- [24] P. G. Moschopoulos, "The distribution of the sum of independent gamma random variables," *Annals of the Institute of Statistical Mathematics*, vol. 37, no. 1, pp. 541–544, 1985.
- [25] M. Nakagami, "The m-distribution—A general formula of intensity distribution of rapid fading," in *Statistical methods in radio wave propagation*. Elsevier, 1960, pp. 3–36.
- [26] (2016) Hoytdistribution. Wolfram Research. [Online]. Available: <https://reference.wolfram.com/language/ref/HoytDistribution.html>
- [27] G. Tavares, "Efficient computation of Hoyt cumulative distribution function," *Electronics letters*, vol. 46, no. 7, pp. 537–539, 2010.